CrossMark

# The Impact of Sub-Resolution Porosity of X-ray Microtomography Images on the Permeability

Cyprien Soulaine[1] · Filip Gjetvaj[2] · Charlotte Garing[1] · Sophie Roman[1] ·
Anna Russian[2] · Philippe Gouze[2] · Hamdi A. Tchelepi[1]

**Abstract** There is growing interest in using advanced imaging techniques to describe the complex pore-space of natural rocks at resolutions that allow for quantitative assessment of the flow and transport behaviors in these complex media. Here, we focus on representations of the complex pore-space obtained from X-ray microtomography and the subsequent use of such 'pore-scale' representations to characterize the overall porosity and permeability of the rock sample. Specifically, we analyze the impact of sub-resolution porosity on the macroscopic (Darcy scale) flow properties of the rock. The pore structure of a rock sample is obtained using high-resolution X-ray microtomography ($3.16^3 \, \mu m^3$/voxel). Image analysis of the Berea sandstone sample indicates that about 2 % of the connected porosity lies below the resolution of the instrument. We employ a Darcy–Brinkman approach, in which a Darcy model is used for the sub-resolution porosity, and the Stokes equation is used to describe the flow in the fully resolved pore-space. We compare the Darcy–Brinkman numerical simulations with core flooding experiments, and we show that proper interpretation of the sub-resolution porosity can be essential in characterizing the overall permeability of natural porous media.

## 1 Introduction

Improvements in imaging technologies and step changes in computing power are making it possible to image natural porous media with high resolution. Digitized images of the complex pore-space in three dimensions (3D) are often used to analyze the flow dynamics and compute

✉ Cyprien Soulaine
csoulain@stanford.edu

1 Energy Resources Engineering, Stanford University, 367 Panama St., Stanford, CA 94305, USA

2 Géosciences Montpellier, UMR 5243 CNRS/INSU, Université de Montpellier 2, 34095 Montpellier, France

flow-related quantities, such as permeability, relative permeability, and capillary–pressure relations. The process of imaging natural rocks and modeling the flow dynamics using the high-resolution representations of the pore-space is often referred to as digital rock physics. The application areas include reservoir engineering, subsurface hydrology, and subsurface $CO_2$ sequestration. Specifically, X-ray microtomography (micro-CT) permits 3D imaging of the pore structure of rock samples that are a few cubic millimeters in size at a resolution a micron (e.g., images made up of $2000^3$ voxels with a voxel size of one cubic micrometer; Wildenschild and Sheppard 2013; Blunt et al. 2013). On the flow simulation side, the computational fluid dynamics (CFD) community has invested significant efforts to develop flexible and computationally efficient software platforms for high-resolution numerical simulation of complex flows. Combined with modern high-performance computing (HPC) architectures and solution algorithms, CFD flow simulators can employ models with complex 3D grids on the order of a billion cells (Trebotich and Graves 2015). Numerical solutions of the Stokes equations using realistic representations of the 3D pore geometry, which can be obtained from micro-CT images, are used to obtain the (single-phase) velocity **v** field in the pore-space. Computation of the pressure and velocity fields for single-phase flow at the pore-scale is used to obtain the permeability tensor, K, of a representative elementary volume (REV) of porous structures (Spanne et al. 1994; Arns et al. 2005; Kainourgiakis et al. 2005; Zhan et al. 2009; Khan et al. 2011; Thovert and Adler 2011; Blunt et al. 2013; Mostaghimi et al. 2013; Andrä et al. 2013a, b; Guibert et al. 2015b).

Many natural rocks, such as carbonates, have pore-spaces with complex heterogeneities that span a very wide range of scales. A fraction of the pore-network may have features that are smaller than the voxel size. This is the case even with the most advanced micro-CT devices (e.g., synchrotron-based micro-CT with a voxel size below 500 nm; Arns et al. 2005; Garing et al. 2014; Hebert et al. 2015). For natural rocks that exhibit multimodal pore-size distributions, the 'segmentation' of the raw images is a crucial step, since different methods can lead to very different pore-space geometries. Multithresholding segmentation algorithms improve the quality of differentiation. Nevertheless, one ends up with three classes: voxels occupied completely by solid minerals, voxels that represent void space, and voxels that are below the instrument resolution. This last category, which may be composed of solid material, void space, or both, is referred to as micropores. Ignoring such microporosity can lead to a significant underestimation of the overall pore-space connectivity, as illustrated in Fig. 1. The red and blue regions in the figure correspond to zones that are unambiguously identified as void and solid phases, respectively; the purple and green areas denote microporous zones. If during the segmentation process the purple region is identified as a solid phase, then the flow resistance in the highlighted throat will be overestimated. This interpretation would lead to less flow through this particular area and more flow through the adjacent pore-throats. If such complex features are present across the 3D space, the erroneous distribution of the preferential flow paths can lead to significant errors in characterizing the flow capacity of the rock. It is also possible for microporous material to act as connecting macropores, as illustrated by the green region in Fig. 1. It follows that 'bad' segmentation of the raw image can misrepresent the degree of connectivity. That, in turn, is likely to lead to significant errors in the computed local velocity field, **v**, and produce significant errors in assessing the overall permeability of the sample. Such complexities are not restricted to carbonates. For example, it has been demonstrated that Berea sandstones may contain between 2 and 10 % of microporosity (Churcher et al. 1991; Tanino and Blunt 2012).

For example, non-Fickian dispersion in natural rocks has been attributed—in part—to diffusion in the microporous matrix (see Gouze et al. 2008, and reference therein). Most of the works published so far assume that diffusion is the primary transport mechanism in the
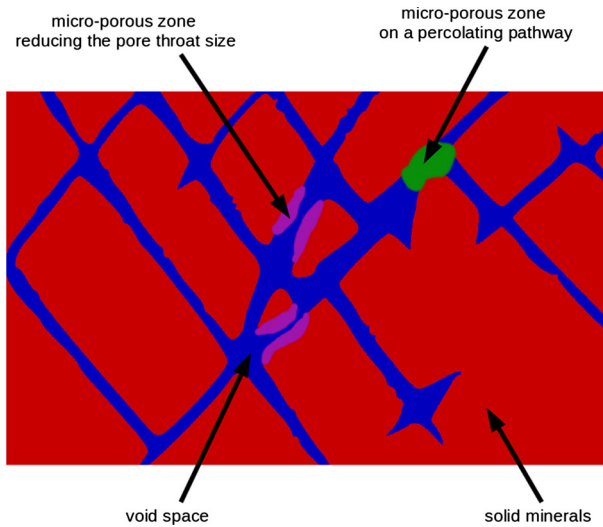
**Fig. 1** Schematic of a micro-CT rock sample image. The *red* and *blue regions* are identified as solid minerals and void spaces, respectively. The *green* and *purple areas* denote microporous regions

microporosity (Haggerty and Gorelick 1995; Carrera et al. 1998; Gouze et al. 2008; Shabro 2011; Gjetvaj et al. 2015). The validity of this assumption is questionable, especially if the microporous region is located in a percolating pathway, as illustrated by the green area in Fig. 1. In such a case, convection in the microporous region may play an important role and should be included into the modeling of tracer transport. To capture the multiscale nature of the pore-space, the microporous regions can be represented using parallel bonds in a pore-network model (PNM; Ioannidis and Chatzis 2000; Bekri et al. 2005; Youssef et al. 2008; Bauer et al. 2011; Jiang et al. 2013; Mehmani and Prodanović 2014; Bultreys et al. 2015; Prodanović et al. 2015). With such a technique, often referred to as a dual PNM, the macroporosity is treated using a standard PNM reconstructed from the micro-CT images, and the microporous bonds are considered as continuum porous medium. The dual PNM representation is easily extended to the flow of multiple fluid phases (e.g., oil and water). One of its main drawback, however, is inherent to PNM, namely, that the extracted pore-network is an approximation of the real pore structure, and the results of the flow simulations depend strongly on the transport/invasion rules used for the nodes and the connections.

We employ a strategy that allow us to compute the flow field in the fully resolved pore-space and also account for the presence of microporous regions. Such regions are defined as material that may contain pores whose size is smaller than the voxel size, which depends on the imaging device. Specifically, we describe a hybrid approach that solves the Stokes equations in the regions identified as pore (void) space and Darcy's law for flow in the microporous domain. The Darcy–Brinkman approach has been used effectively to compute accurate flow fields in bimodal porosity distributions (Knackstedt et al. 2006; Apourvari et al. 2014; Krotkiewski et al. 2011; Scheibe et al. 2015). Particular attention must be paid to the estimate of the permeability of the microporous domain, $k_{micro}$. In the absence of additional knowledge about the geometrical structure of the sub-resolution (sub-voxel) porosity (e.g., from higher image resolution), $k_{micro}$ has to be modeled based on the available image resolution. At minimum, the permeability should be expressed as a function of the image resolution and the associated maps of the microporous regions.

Next, we describe the rock sample used in this study, including the imaging method and the data processing used to determine the different components (i.e., void, solid, and microporous region). Then, we present a Darcy–Brinkman formulation, including a heuristic relation for estimating $k_{\text{micro}}$ from the porosity of the microporous phase obtained from the X-ray microtomography images. Then, the numerical simulations of eight sub-volumes of the scanned rock sample are presented, and the impact of the microporosity on the distribution of the velocity field and the estimation of the overall permeability are discussed.

## 2 Materials and Methods

This section introduces the X-ray microtomography technique used to scan the Berea sandstone sample, the mathematical model developed to obtain the velocity distribution in the void space, and the setup for the flow simulations.

### 2.1 X-ray Microtomography

X-ray microtomography is a noninvasive imaging technique that allows for constructing a 3D image of the target object using a set of two-dimensional (2D) radiographs of the X-ray attenuation properties of the material that makes up the object. Each 'voxel' value corresponds to a measure of linear-absorption coefficients, which for a porous medium depends on the porosity and the composition of the solid matrix.

#### 2.1.1 Sample

We study a Berea sandstone sample obtained from a larger block with overall porosity and permeability values of 0.20 and 500 mD, respectively. A mercury intrusion porosimetry test (AutoPore IV 9500 V1.06 from Micromeritics Instrument Corporation) was conducted on a sample cored out from a nearby location; the mercury-injection test yields an overall porosity of 19.41 % and a mean pore-throat diameter of 11.7 μm. The curve of the differential intrusion, which can be related to the pore-throat size distribution, is shown in Fig. 2. The limit size separating the 'macropores' (diameter above 3.16 μm) from the 'micropores' (diameter below 3.16 μm) is also shown. The figure suggests that the fraction of microporous material in the sample is quite small.

#### 2.1.2 Data Acquisition

The sample of 6 mm diameter and 6 mm length was imaged at the BM5 beamline of the European Synchrotron Radiation Facility (ESRF), Grenoble, France. Synchrotrons provide very high flux of the monochromatic white beam and collimated X-rays resulting in high-quality, low-noise images with a resolution of a few microns. A total of 3495 projections of the sample were taken, every 0.051° for angles from 0° to 180° using an exposure time of 0.1 s and an X-ray beam energy of 30 keV. The voxel size was $3.16\,\mu\text{m}^3$.

The radiographs were corrected for variations in the X-ray beam intensity and background noise. Then, the 3D volume of $4667 \times 2130 \times 2099$ voxels was constructed from the radiographs using a single-distance phase-retrieval algorithm (Paganin et al. 2002; Sanchez et al. 2012). Figure 3a presents a numerically computed cross section through the 3D volume. The black color denotes the 'macroporosity' phase (void only), the lighter gray denotes the solid matrix, and the intermediate gray levels denote the microporous phase (voxels composed of
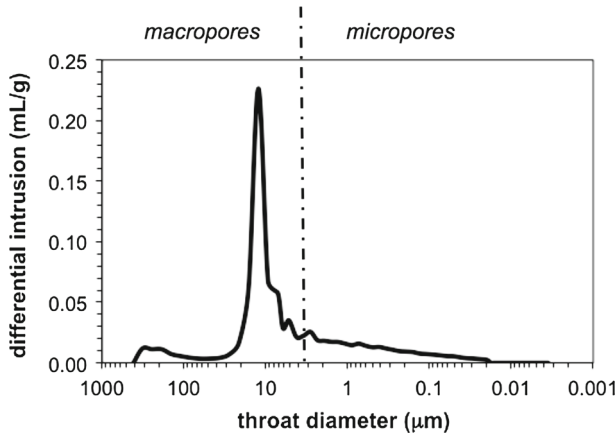
**Fig. 2** Pore-throat size distribution of the studied Berea sandstone determined from a mercury-injection test (presented as the differential intrusion). The limit pore-size separating macropores and micropores in this study (3.16 microns) is displayed as a *dashed line*
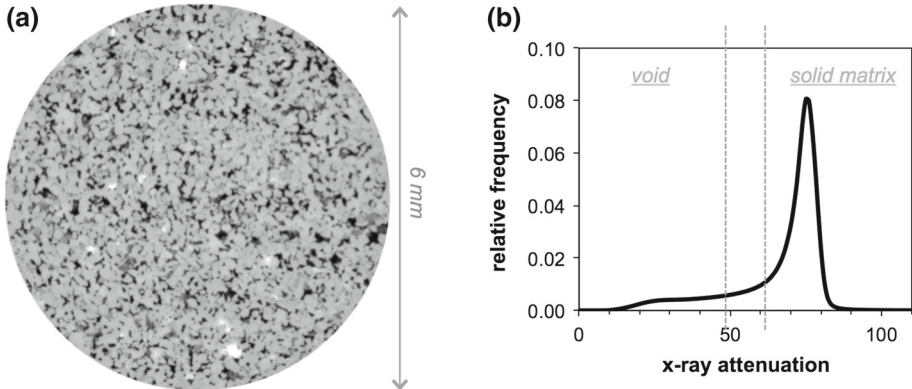


**Fig. 3** **a** Cross section through the 3D volume. **b** X-ray attenuation histogram for the entire sample

both solid and void). The X-ray attenuation histogram for the entire sample is displayed in Fig. 3b, which shows an intermediate attenuation range between the pore and the solid peaks that can be designated as a microporous phase.

### 2.1.3 Data Processing

In order to quantify the volume fraction and distribution of each phase, the grayscale images must be segmented, such that each phase is identified by a single integer. Since the gray-level histogram (Fig. 3b) does not show well-separated peaks characterizing the pore and solid phases, a three-phase segmentation approach is used to identify the microporous phase. This was done using the iterative growing-region algorithm described in Noiriel et al. (2005) with two sets of threshold values. A one-voxel erosion was performed when distinguishing between voids (macroporosity) and the rest of the sample in order to remove edge artifacts that would then be incorporated in the microporous phase. The fractions of the different phases are: 79.45, 18.15, and 2.4 % for the solid, macroporosity, and microporous phases,
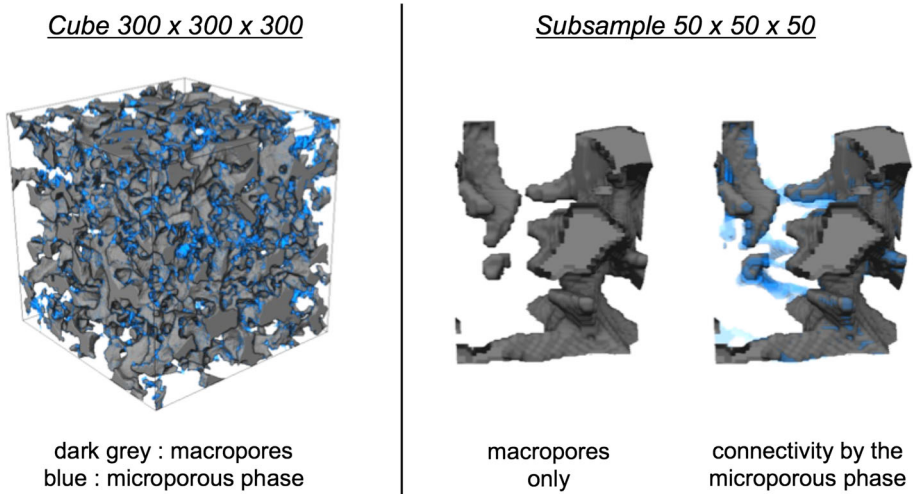
**Fig. 4** Three-dimensional representation of the connected macroporosity and microporous phases on a cube of $300 \times 300 \times 300$ voxels (*left*) and close-up of macropores that are only connected through microporous material (*right*)

respectively. The microporosity has a mean intrinsic porosity of 49.4 %, leading to a total porosity of 19.36 % for the entire sample.

Six cubic sub-volumes of $300 \times 300 \times 300$ voxels ($0.948^3\,\text{mm}^3$) and two of $350 \times 350 \times 350$ voxels ($1.11^3\,\text{mm}^3$) were extracted from different locations within the 3D image representing the entire sample. For each sub-volume, the connectivity of the macroporosity and microporous phases was investigated using a modified version of the Hoshen–Kopelman algorithm ([1976](#)). The fractions of the connected macropores and of the total connected porous network, considering that the micropores comprised in the connected part of the microporous phase are also well connected, are detailed in Table 3 for all sub-volumes. The connected porosity (macropores and micropores) ranges from 17.9 to 21.0 %, with a mean value around 19.8 %. A close look at the distribution of the connected phases within the sub-volumes indicates that some macropores are only connected through microporous material, as shown in Fig. 4.

## 2.2 Mathematical Model

Once the image processing is complete, the solid structure is mapped by the microporosity field, $\varepsilon_{\text{micro}}$, which varies between 0 to 1 and corresponds to the void fraction in each voxel. If $\varepsilon_{\text{micro}} = 1$, the voxel contains void only, and the flow is governed by the Stokes equation. If $\varepsilon_{\text{micro}} = 0$, the cell is entirely composed of solid minerals, and there is no fluid flow. Intermediate values, i.e., $0 < \varepsilon_{\text{micro}} < 1$, denote microporous regions whose characteristic length scale is below the voxel size. In these sub-resolution microporous regions, the flow is modeled using Darcy's law. To simulate flow in a volume that includes microporosity (i.e., microporous regions), we use a single-domain approach, whereby a single equation, namely the Darcy–Brinkman formulation (Brinkman 1947), holds for both the free-flow and the porous medium regions. The model arises from the integration of Stokes equations over a control volume (here, a voxel) in the presence of solid material (John 1969; Whitaker 1986). Having a single conservation equation makes stresses and velocities continuous through-

out the entire domain. Thus, changes across the transition zone are captured using spatial variations of properties, such as permeability and porosity (Neale and Nader 1974).

Since the microporosity field, $\varepsilon_{\text{micro}}$, denotes the average amount of void in each voxel, one can define the voxel-averaged pressure and velocity fields, $\bar{p}$ and $\bar{\mathbf{v}}$ as:

$$\bar{\mathbf{v}} = \frac{1}{V_{\text{voxel}}} \int_{V_{\text{voxel}}} \mathbf{v} \, dV \quad \text{and} \quad \bar{p} = \frac{1}{V_{\text{voxel}}} \int_{V_{\text{voxel}}} p \, dV. \tag{1}$$

These two variables satisfy the locally averaged Stokes equations (Whitaker 1986),

$$\nabla \cdot \bar{\mathbf{v}} = 0, \tag{2}$$

and

$$0 = -\nabla \bar{p} + \frac{\mu}{\varepsilon_{\text{micro}}} \nabla^2 \bar{\mathbf{v}} - \mu k_{\text{micro}}^{-1} \bar{\mathbf{v}}, \tag{3}$$

where the latest term of the right-hand side of Eq. (3) is a drag force. This momentum-exchange term between the fluid and solid phases is represented using the standard Darcy form. It is meaningful only if the voxel contains solid minerals. Conversely, if the control volume is occupied by fluid only, there is no friction of the fluid against any solid structure, and this 'drag' term approaches zero. The drag force coefficient, $k_{\text{micro}}$, represents the permeability of the microporous regions, which is denoted as micropermeability. It is a function of $\varepsilon_{\text{micro}}$, such that the resistance flow term $\mu k_{\text{micro}}^{-1} \bar{\mathbf{v}}$ vanishes in the free zone and is dominant in the microporous medium. With such considerations, the locally averaged Stokes momentum equation, Eq. (3), tends toward:

– Stokes when $\varepsilon_{\text{micro}} = 1$. In that case, $\bar{\mathbf{v}} = \mathbf{v}$,
– Darcy when $0 < \varepsilon_{\text{micro}} < 1$. In that case, the resistance flow term is dominant (Tam 1969; Auriault 2009) and $\bar{\mathbf{v}} = -\frac{k_{\text{micro}}}{\mu} \nabla \bar{p}$.

In summary, below a certain resolution imposed by the image acquisition setup and the sample size, the solid structure is modeled by a microporous medium. We can imagine a multiscale approach where a very high-resolution imaging of the microporosity allows for an estimate of its local micropermeability. However, this kind of approach is costly and requires advanced equipment such as a laboratory nano-CT. Instead, for a given voxel, we can use the information of the image acquisition process, namely its size and the volume fraction of void in the voxel to estimate the microporosity. The Kozeny–Carman equation,

$$k_{\text{micro}}^{-1} = \frac{180}{d^2} \frac{(1 - \varepsilon_{\text{micro}})^2}{\varepsilon_{\text{micro}}^3}, \tag{4}$$

serves as an appropriate model, since $k_{\text{micro}}^{-1} \to \infty$ for very low values of the microporosity (solid only) and $k_{\text{micro}}^{-1} = 0$ in the free zone. In Eq. (4), $d$ represents a characteristic length, which is usually associated with the grain size. In the absence of additional information, $d$ is associated with the voxel size; this leads to overestimating the characteristic length scale and the micropermeability. Except perhaps in the case where the microporous region is located around percolating pathways (green region in Fig. 1), the main contribution to the permeability, $\mathsf{K}$, comes from the macropores, which are explicitly represented in this approach (blue regions in Fig. 1). Therefore, a gross approximation of the micropermeability is not expected to have a strong impact on the overall permeability. It is worth noting that the two asymptotic values of the micropermeability $k_{\text{micro}}^{-1} = 0 \, \text{mD}^{-1}$ (fully permeable) and $k_{\text{micro}}^{-1} = \infty \, \text{mD}^{-1}$ (impermeable) define bounding configurations regardless of the microporosity/micropermeability relationship, $k_{\text{micro}} = \text{f}(\varepsilon_{\text{micro}})$; therefore, they define bounding values for the permeability, $\mathsf{K}$.

The porosity and permeability can be deduced from these simulations by integration of the results over the sample volume, $V$. The porosity of the medium is expressed as:

$$\varepsilon = \frac{1}{V} \int_V \varepsilon_{\text{micro}} \mathrm{d}V, \tag{5}$$

and the components of the absolute permeability tensor in the $j$-axis are written as:

$$K_{ij} = \mu \left( \frac{\Delta P}{L} \right)_j^{-1} \left( \frac{1}{V} \int_V \bar{v}_i \mathrm{d}V \right) \quad \text{with} \quad i = x, y, z, \tag{6}$$

where $\left( \frac{\Delta P}{L} \right)_j$ is the pressure loss in the $j$ direction. To obtain the full tensor, three simulations are required: $j = x, y, z$. In the present study, however, only the main component in $z$-axis, $K_{zz}$, is investigated.

## 2.3 Numerical Implementation and Simulation Setup

The mathematical model formed by Eqs. (2) and (3) can be easily solved in the framework of the semi-implicit method for pressure-linked equations (SIMPLE) algorithm (Patankar 1980). This algorithm is an iterative procedure for solving the steady-state equations for velocity and pressure. To improve the stability of the computations, under-relaxation parameters, $\alpha_p$ and $\alpha_U$ must be specified. The first one limits the amount of pressure changes from one iteration to the next by modifying the pressure field directly. The second parameter limits the amount of velocity variation by under-relaxing the solution matrix prior to solving for the velocity field. This algorithm is embedded in most CFD software, so the effort to implement the model is quite small. In the present study, the finite-volume toolbox OpenFOAM® (http://www.openfoam.org) is used. The SIMPLE solver of this package, *simpleFoam*, which has been shown to have good scalability for parallel computing of single-phase flow in the pore-space (Guibert et al. 2015b), is customized to incorporate the flow resistance term, $\mu k_{\text{micro}}^{-1} \bar{\mathbf{v}}$, into the momentum equation. For improved stability, this term is treated as an implicit source term adding its contribution into the diagonal coefficients of the velocity matrix.

The computational domain is based on the X-ray microtomography segmented image that is cropped as a cube of volume $V$. In order to save computational time and memory, the voxels that are identified as containing solid only, i.e., $\varepsilon_{\text{micro}} = 0$, are represented as boundaries with a no-slip condition at the solid/fluid interface. The boundary conditions at the edges of the computational domain are set to mimic an experimental permeameter: A pressure difference, $\Delta P_z$, is imposed on the inlet and outlet sides of the sample, and no-flow conditions are specified on the other faces of the samples (Guibert et al. 2015a, b). To specify these inlet and outlet boundary conditions, the computational domain is complemented with two manifolds of $21 \, \mu\text{m}$ thick. Since there is no-flow resistance in these manifolds, the pressure drop in the boundary regions can be neglected compared with the pressure loss through the porous structure. Hence, the overall pressure drop in the rock sample is $\frac{\Delta P_z}{L_z}$, where $L_z$ denotes the length of the sample in the $z$ direction without the manifolds. The mean velocity used to estimate the permeability with Eq. (6) is computed excluding the velocity distribution in the manifolds.

The gridding process is a major step considering its strong influence on the accuracy of the computations. Previous studies have based their computational grids directly on the image voxels, i.e., one cell of the simulation grid corresponds to one voxel of the micro-CT image (Arns et al. 2005; Mostaghimi et al. 2013). However, because a porous medium skeleton

**Table 1** Mesh convergence study performed on a $150^3$ voxels sub-volume of the scanned Berea sandstone sample

| $n$ | 1 | 2 | 3 | 4 | 5 | 6 | 7 |
|---|---|---|---|---|---|---|---|
| $K_{zz}$ (mD) | 736 | 657 | 630 | 617 | 610 | 605 | 602 |
| SD (%) | 22.4 | 9.1 | 4.7 | 2.5 | 1.3 | 0.5 | 0 |

consists of numerous narrow throats, one has to ensure that the smallest throat contains enough cells in order to get an accurate flow profile. Guibert et al. (2015b) performed mesh convergence analysis to investigate the influence of the size of the mesh on the simulation results; they reported that a computational grid made of the image voxels can exhibit up to 50 % relative error in terms of the computed overall permeability. Table 1 summarizes the mesh convergence study we performed on a $150^3$ voxels sub-volume of the scanned Berea sandstone sample. The sub-volume does not contain any microporous regions. In this study, the image voxels were divided by $n^3$ with $n$ varying from 1 to 7. Without refinement, a computational grid based on the image voxels only leads to up to 22 % error in the absolute permeability. This preliminary study leads us to choose simulation grids consisting of cells $3^3$ finer than the image voxels, which offers a good compromise between accuracy (less than 5 % error) and simulation cost.

The computational domain is decomposed into 256 sub-domains, and simulations are carried out in parallel with 256 cores on Stanford Center for Computational Earth and Environmental Sciences cluster, 148 compute nodes, Dual E5-2660 Intel cpus (8 cores, 2.2 GHz 8.0 GT/s 20 mb 95 W DDR3-1600), 64 GB memory. Convergence is considered reached when the residuals go below $10^{-6}$. The relaxation factors $\alpha_p$ and $\alpha_U$ are set to 0.2 and 0.9, respectively. Indeed, we noticed that for the Stokes problem, the simulations require up to twice less iterations to converge to the solution with $\alpha_U = 0.9$ as with the usual recommended value $\alpha_U = 0.8$. In every case, the simulations converge to the solution within 2 h.

## 3 Results and Discussion

This section presents the simulation results for the different sub-volumes. We first study the influence of the sub-voxel porosity on the pore-scale simulation results. We show that even with only 2 % of microporosity the computed permeability can be far from the 'true' value, if the image is not segmented properly and the sub-voxel porosity is not accounted for in the flow modeling. Then, simulation results of single-phase flow in the eight sub-volumes of the Berea sandstone sample with distributed microporosity throughout the domain are presented and discussed.

### 3.1 Influence of Sub-Voxel Porosity

To investigate the influence of microporosity on pore-scale flow simulations, a sub-volume of the image, denoted SubV0, was extracted and segmented into three different phases: void, solid, and microporous. The connected pore structure of this sub-volume corresponds to 19.7 % of macroporosity and 2.6 % of microporosity. Regions identified as microporous are colored in red in Fig. 5a. We observe that in some areas, according to the value of microporosity, $\varepsilon_{micro}$, some pathways can switch from percolating to non-percolating. In this part, it is assumed that the value of $\varepsilon_{micro}$ is the same for all the voxels identified as a microporous phase.
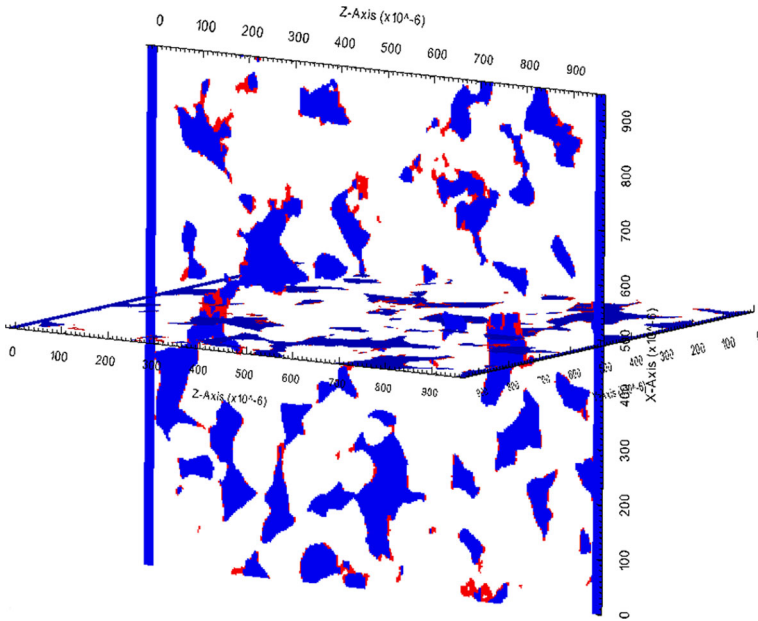
**Fig. 5** Map of the microporous regions for subsample SubV0 (*blue* = void, *red* = microporosity)

**Table 2** Summary of simulation results for different microporosity values

| $\varepsilon_{\text{micro}}$ | 0.001 | 0.25 | 0.5 | 0.75 | 0.9 | 1 |
|---|---|---|---|---|---|---|
| $k_{\text{micro}}$ (mD) | 0 | 2 | 27 | 365 | 3944 | $\infty$ |
| $\varepsilon$ | 0.197 | 0.204 | 0.210 | 0.216 | 0.220 | 0.223 |
| $K_{zz}$ (mD) | 702 | 798 | 839 | 950 | 1168 | 1366 |

Micropermeability, $k_{\text{micro}}$, is estimated with Eq. (4). The permeability obtained when the microporosity is distributed based on the gray level is 858 mD

Several simulations are performed for $\varepsilon_{\text{micro}}$ ranging from 0.001 to 1. For these two extremes, the computed permeability is 702 and 1366 mD, respectively. These two limit values of $\varepsilon_{\text{micro}}$ denote specific situations, whereby the microporous phase is identified as fully solid ($\varepsilon_{\text{micro}} = 0.001$) or fully void ($\varepsilon_{\text{micro}} = 1$). Because of the asymptotic values of the associated micropermeability, $k_{\text{micro}}^{-1} = 0$ or $\infty$ mD$^{-1}$ for these two bounding cases (here, $\infty$ stands for $10^7$ mD$^{-1}$, which ensures that there is no flow in the microporous zone when $\varepsilon_{\text{micro}} = 0.001$), the resulting velocity distributions, and thus the permeability, are independent of the relation between the microporosity and micropermeability.

Table 2 presents the computed permeability, $K_{zz}$, and porosity, $\varepsilon$, of SubV0 for different values of the microporosity. As expected, $K_{zz}$ increases when the pore-throats size is larger, i.e., for higher value of microporosity. The results clearly show that according to the segmentation process, the computed absolute permeability can be up to twice larger, or smaller, than the actual value. For this subsample, the permeability value obtained when the microporosity is distributed and proportional to the gray level lies between the bounding values and was estimated to be 858 mD.
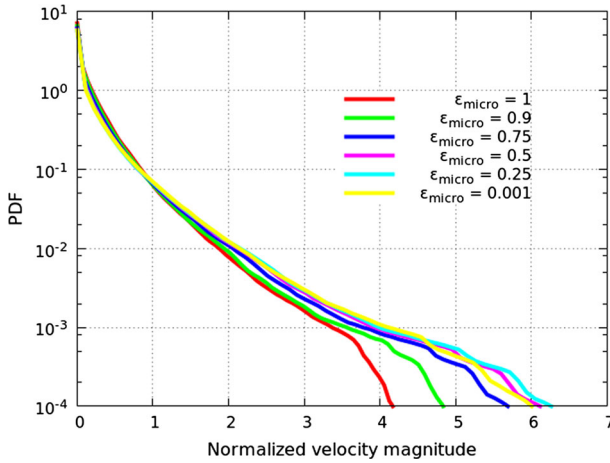
**Fig. 6** Probability density functions of the normalized velocity distribution for $\varepsilon_{\mathrm{micro}}$ ranging from 0 to 1

The probability density functions (PDFs) of the normalized velocity distribution, $\frac{|\bar{\mathbf{v}}|}{\left|\frac{1}{V}\int_V \bar{\mathbf{v}} dV\right|}$, are plotted for different values of $\varepsilon_{\mathrm{micro}}$ in Fig. 6. In all cases, 99 % of the cells contains velocities up to twice the superficial mean velocity and the PDFs present a quasi-exponential decay reminiscent of recent numerical and experimental works (Anna et al. 2013; Datta et al. 2013). About 0.9 % contains velocity between two and four times the mean velocity. The PDFs are shifted toward the right as the microporosity value gets reduced. Below a certain threshold, here close to $\varepsilon_{\mathrm{micro}} = 0.75$, the PDFs become indistinguishable. This suggests that for simulations above this value ($\varepsilon_{\mathrm{micro}}$ from 0.75 to 1), the presence, or absence, of microporous regions significantly changes the flow pathways. This means that some of the gray regions are located where their impact on the flow is quite significant. The flow resistance in this area becomes so important that it locally redistributes the flow, favoring other pores. On the contrary, for simulations with $\varepsilon_{\mathrm{micro}}$ below 0.75, the flow pathways are always the same, regardless of the microporosity value. In such cases, the magnitude of the velocity field increases with the reduction of the pore-space, as expected. The velocity profiles plotted in Fig. 7 illustrate this situation. According to Kozeny–Carman correlation applied to the subsample, a change of porosity from 0.197 to 0.223 predicts a permeability increase by about 50 %. Our results show a more significant increase that can be explained by the local redistribution of the flow due to microporosity.

### 3.2 Simulation Results for Distributed Microporosity

The situation presented so far whereby the value of the sub-voxel porosity is the same throughout the entire rock sample is not realistic. It was used to emphasize that if the length scales below the image resolution are not considered in the flow modeling, then the velocity distribution obtained form the pore-scale simulation can be inaccurate. In general, the microporosity has values that are heterogeneously distributed in the rock. In this section, the microporosity domain, $\varepsilon_{\mathrm{micro}}$, is defined as a distribution of porosity values, and subsequently a distribution of permeability values using Eq. (4), obtained from the distribution of the gray level in the microporous phase (see an example in Fig. 8a). The velocity distributions and permeability of the eight sub-volumes are computed according to the procedure described in Sect. 2. The
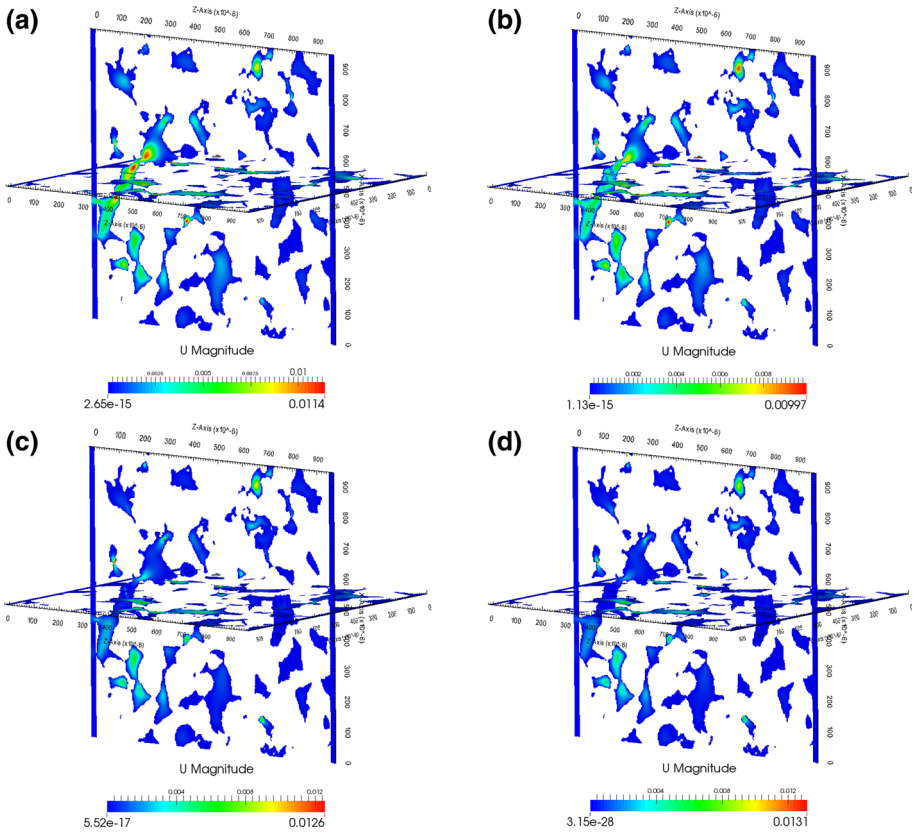
**Fig. 7** Plot of the velocity distribution for different sub-voxel porosity values: **a** $\varepsilon_{\mathrm{micro}} = 1$, **b** $\varepsilon_{\mathrm{micro}} = 0.9$, **b** $\varepsilon_{\mathrm{micro}} = 0.5$, **d** $\varepsilon_{\mathrm{micro}} \approx 0$

computational grid for the six cubes of $300 \times 300 \times 300$ voxels and for the two cubes of $350 \times 350 \times 350$ voxels contain approximately $220 \times 10^6$ and $330 \times 10^6$ cells, respectively.

Figure 8b, c displays the velocity–magnitude distribution and the pressure field in the void space of a $300 \times 300 \times 300$ voxels sub-volume. These simulation results are then volume averaged following Eq. (6) to deduce the permeability of the different sub-volumes. Table 3 summarizes the simulation results for the different investigated sub-volumes. The calculated porosity is $0.20 \pm 0.02$, as measured in laboratory on the Berea sandstone rock sample. Computed permeabilities range from 341 to 858 mD, and the mean value of the eight simulations is 672 mD. These results are in good agreement with the 500 mD given by core measurements. The permeability and porosity bounding values were also computed following the methodology introduced in the previous section: the upper bounds, $K^+$ and $\varepsilon^+$, are obtained when the gray values are set to void, and the lower bounds, $K^-$ and $\varepsilon^-$, are obtained when the gray values are assimilated to solid. The corresponding values are reported in Table 3. The results highlight that in some cases $K^-$ underestimates the permeability by almost 60 % (SubV4) and $K^+$ overestimates the permeability value by 100 % (SubV6). In average, the computed permeability can be underestimated by 18 % when the zones presenting intermediate gray-level values are considered as solid and overestimated by 60 % when these zones are assigned as void space. Although the studied Berea sandstone contains approximately
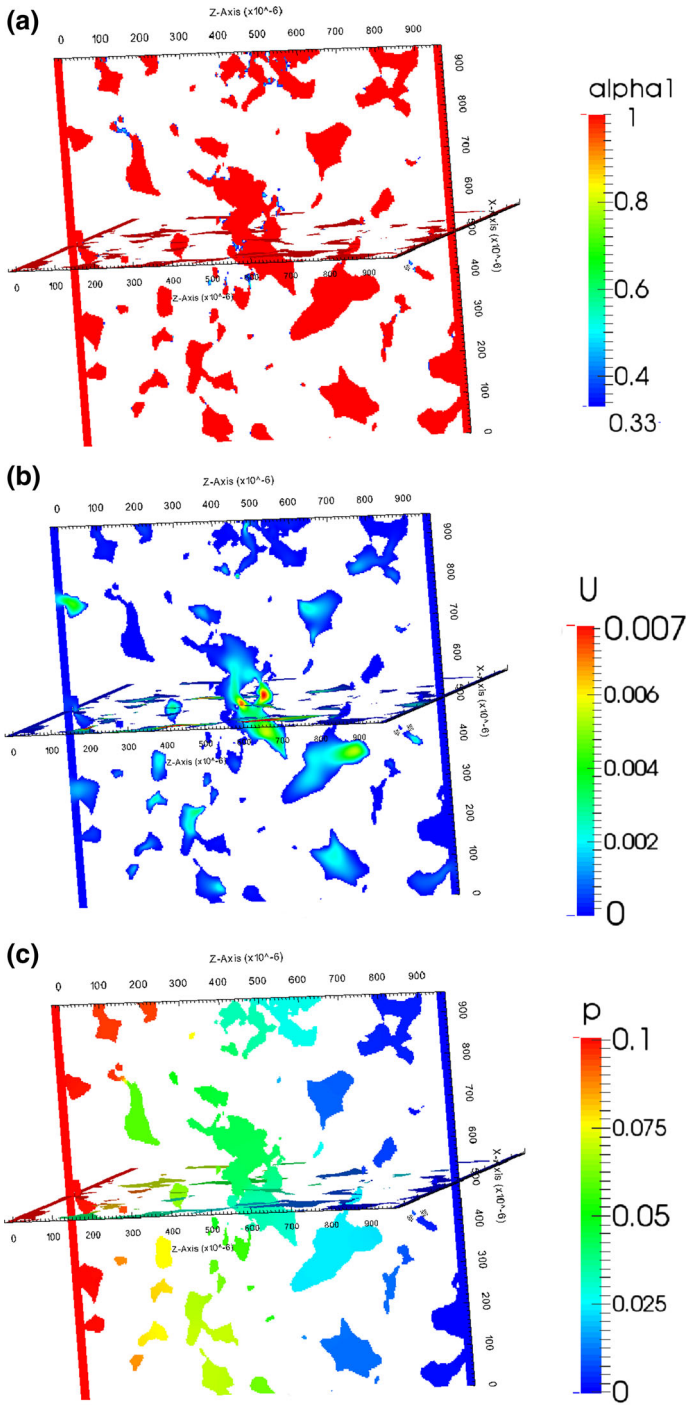
**Fig. 8** Plot of the simulation results for a $300 \times 300 \times 300$ voxels sub-volume. **a** Microporosity distribution, **b** velocity distribution, **c** pressure field

**Table 3** Values of porosity and permeability computed for the different sub-volumes

| Sample | SubV1 | SubV2 | SubV3 | SubV4 | SubV5 | SubV6 | SubV7 | SubV8 |
|---|---|---|---|---|---|---|---|---|
| Resolution | $300 \times 300 \times 300$ | | | | | | $350 \times 350 \times 350$ | |
| $\varepsilon$ | 0.210 | 0.208 | 0.197 | 0.199 | 0.193 | 0.178 | 0.197 | 0.199 |
| $K_{zz}$ (mD) | 858 | 848 | 785 | 518 | 534 | 341 | 659 | 835 |
| $\varepsilon^-$ | 0.197 | 0.196 | 0.186 | 0.187 | 0.183 | 0.166 | 0.187 | 0.188 |
| | $(-6.2\,\%)$ | $(-5.8\,\%)$ | $(-5.6\,\%)$ | $(-6\,\%)$ | $(-5.2\,\%)$ | $(-6.7\,\%)$ | $(-5.1\,\%)$ | $(-5.5\,\%)$ |
| $\varepsilon^+$ | 0.222 | 0.220 | 0.208 | 0.213 | 0.203 | 0.191 | 0.207 | 0.211 |
| | $(+5.7\,\%)$ | $(+5.8\,\%)$ | $(+5.6\,\%)$ | $(+7\,\%)$ | $(+5.2\,\%)$ | $(+7.3\,\%)$ | $(+5.1\,\%)$ | $(+5.5\,\%)$ |
| $K^-$ (mD) | 792 | 762 | 681 | 211 | 475 | 305 | 547 | 738 |
| | $(-8\,\%)$ | $(-10\,\%)$ | $(-13\,\%)$ | $(-59\,\%)$ | $(-11\,\%)$ | $(-11\,\%)$ | $(-17\,\%)$ | $(-12\,\%)$ |
| $K^+$ (mD) | 1365 | 1313 | 1150 | 913 | 804 | 673 | 1053 | 1277 |
| | $(+59\,\%)$ | $(+55\,\%)$ | $(+46\,\%)$ | $(+76\,\%)$ | $(+51\,\%)$ | $(+97\,\%)$ | $(+60\,\%)$ | $(+53\,\%)$ |

Superscripts $-$ and $+$ correspond to the lower and upper bounding values. In average, the SD for $K^-$ is $-18\,\%$ and the SD for $K^+$ is $+62\,\%$
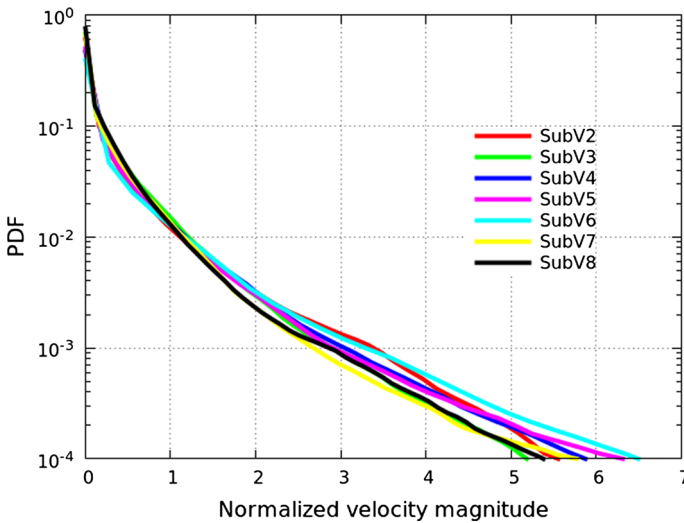


**Fig. 9** Probability density functions of the velocity distribution for the different sub-volumes

2 % of sub-voxel porosity, its influence on permeability computation is already significant. A higher impact is expected for complex multiscale rocks such as carbonates that are likely to present a high ratio of microporosity, and hence may display a significant fraction of sub-voxel porosity, even when imaged with high resolution (Knackstedt et al. 2006; Garing et al. 2014; Hebert et al. 2015).

The probability density functions of the normalized velocity distribution for the different sub-volumes are plotted in Fig. 9. The PDFs display similar trend for all simulations, and 99 % of the cells contains velocities up to 1.5 times the superficial mean velocity. These results confirm that for this Berea sandstone a cube of 1 mm$^3$ can be reasonably considered as a REV large enough to contain all the heterogeneities of the porous medium.

# 4 Conclusions

With improvements of imaging techniques, HPC architectures and simulation capabilities, pore-scale simulations are used to characterize the flow properties of natural porous formations. The foundation of these simulations is a high-resolution representation of the solid skeleton. However, because of the complex, multiple length-scale nature of porous media, some pore structures are much smaller than the image resolution, and they cannot be represented explicitly in the image. In this paper, we proposed a framework based on the Darcy–Brinkman formulation that allows for quantifying the impact of this sub-resolution (sub-voxel) porosity on the pore-scale flow simulations.

Simulations of flow in a Berea sandstone sample have shown that even with only 2 % of microporous regions, the sub-voxel porosity can play an important role in the flow distribution in the pore-space with significant consequences on the computed permeability tensor. In particular, some microporosity regions serve as bridges across macropores, and if such bridges are not represented properly into the modeling, important connectivity can be artificially removed, and the flow capacity of the porous medium would be underestimated. Extension of this Darcy–Brinkman framework to multiple flowing phases is under investigation.

# References

Andrä, H., Combaret, N., Dvorkin, J., Glatt, E., Han, J., Kabel, M., Keehm, Y., Krzikalla, F., Lee, M., Madonna, C., Marsh, M., Mukerji, T., Saenger, E.H., Sain, R., Saxena, N., Ricker, S., Wiegmann, A., Zhan, X.: Digital rock physics benchmarks part I: imaging and segmentation. Comput. Geosci. **50**, 25–32 (2013). Benchmark problems, datasets and methodologies for the computational geosciences

Andrä, H., Combaret, N., Dvorkin, J., Glatt, E., Han, J., Kabel, M., Keehm, Y., Krzikalla, F., Lee, M., Madonna, C., Marsh, M., Mukerji, T., Saenger, E.H., Sain, R., Saxena, N., Ricker, S., Wiegmann, A., Zhan, X.: Digital rock physics benchmarks part II: computing effective properties. Comput. Geosci. **50**, 33–43 (2013). Benchmark problems, datasets and methodologies for the computational geosciences

Apourvari, S.N., Arns, C.H.: An assessment of the influence of micro-porosity for effective permeability using local flux analysis on tomographic images. International Petroleum Technology Conference, Doha, Qatar, 19–22 January 2014

Arns, C.H., Bauget, F., Limaye, A., Sakellariou, A., Senden, T.J., Sheppard, A.P., Sok, R.M., Pinczewski, W.V., Bakke, S., Berge, L.I., Oeren, P.-E., Knackstedt, M.A.: Pore-scale characterization of carbonates using X-ray microtomography. SPE J. **10**(4), 475–484 (2005)

Auriault, J.-L.: On the domain of validity of brinkman's equation. Transp. Porous Media **79**(2), 215–223 (2009)

Bauer, D., Youssef, S., Han, M., Bekri, S., Rosenberg, E., Fleury, M., Vizika, O.: From computed micro-tomography images to resistivity index calculations of heterogeneous carbonates using a dual-porosity pore-network approach: influence of percolation on the electrical transport properties. Phys. Rev. E **84**(1), 011133 (2011)

Bekri, S., Laroche, C., Vizika, O.: Pore network models to calculate transport and electrical properties of single or dual-porosity rocks. In: International symposium of the society of core analysts, Toronto (2005)

Blunt, M.J., Bijeljic, B., Dong, H., Gharbi, O., Iglauer, S., Mostaghimi, P., Paluszny, A., Pentland, C.: Pore-scale imaging and modelling. Adv. Water Resour. **51**, 197–216 (2013)

Brinkman, H.C.: A calculation of the viscous force exerted by a flowing fluid on a dense swarm of particles. Appl. Sci. Res. **A1**, 27–34 (1947)

Bultreys, T., Van Hoorebeke, L., Cnudde, V.: Multi-scale, micro-computed tomography-based pore network models to simulate drainage in heterogeneous rocks. Adv. Water Resour. **78**, 36–49 (2015)

Carrera, J., Sánchez-Vila, X., Benet, I., Medina, A., Galarza, G., Guimerà, J.: On matrix diffusion: formulations, solution methods and qualitative effects. Hydrol. J. **6**(1), 178–190 (1998)

Churcher, P.L., French, P.R., Shaw, J.C., Schramm, L.L., et al.: Rock properties of Berea sandstone, baker dolomite, and Indiana limestone. In: SPE, vol. 21044, pp. 20–22 (1991)

Datta, S.S., Chiang, H., Ramakrishnan, T.S., Weitz, D.A.: Spatial fluctuations of fluid velocities in flow through a three-dimensional porous medium. Phys. Rev. Lett. **111**, 064501 (2013)

De Anna, P., Le Borgne, T., Dentz, M., Tartakovsky, A.M., Bolster, D., Davy, P.: Flow intermittency, dispersion, and correlated continuous time random walks in porous media. Phys. Rev. Lett. **110**(18), 184502 (2013)

Garing, C., Luquot, L., Pezard, P.A., Gouze, P.: Electrical and flow properties of highly heterogeneous carbonate rocks. AAPG Bull. **98**(1), 49–66 (2014)

Gjetvaj, F., Russian, A., Gouze, P., Dentz, M.: Dual control of flow field heterogeneity and immobile porosity on non-Fickian transport in berea sandstone. Water Resour. Res. **51**, 8273–8293 (2015)

Gouze, P., Melean, Y., Le Borgne, T., Dentz, M., Carrera, J.: Non-fickian dispersion in porous media explained by heterogeneous microscale matrix diffusion. Water Resour. Res. **44**, 1–19 (2008)

Guibert, R., Horgue, P., Debenest, G., Quintard, M.: A comparison of various methods for the numerical evaluation of porous media permeability tensors from pore-scale geometry. Math. Geosci. **48**(3), 329–347 (2015)

Guibert, R., Nazarova, M., Horgue, P., Hamon, G., Creux, P., Debenest, G.: Computational permeability determination from pore-scale imaging: sample size, mesh and method sensitivities. Transp. Porous Media **107**, 641–656 (2015)

Haggerty, R., Gorelick, S.M.: Multiple-rate mass transfer for modeling diffusion and surface reactions in media with pore-scale heterogeneity. Water Resour. Res. **31**(10), 2383–2400 (1995)

Hebert, V., Garing, C., Linda, L., Pezard, P.A., Gouze, P.: Multi-scale X-ray tomography analysis of carbonate porosity. Geol. Soc. Lond. Spec. Publ. **406**(1), 61–79 (2015)

Hoshen, J., Kopelman, R.: Percolation and cluster distribution. I. Cluster multiple labeling technique and critical concentration algorithm. Phys. Rev. B **14**(8), 3438 (1976)

Ioannidis, M.A., Chatzis, I.: A dual-network model of pore structure for vuggy carbonates. In: SCA2000-09, International Symposium of the Society of Core Analysts, Abu Dhabi, UAE (2000)

Jiang, Z., Dijke, M.I.J., Sorbie, K.S., Couples, G.D.: Representation of multiscale heterogeneity via multiscale pore networks. Water Resour. Res. **49**(9), 5437–5449 (2013)

Kainourgiakis, M.E., Kikkinides, E.S., Galani, A., Charalambopoulou, G.C., Stubos, A.K.: Digitally reconstructed porous media: transport and sorption properties. In: Das, D.B., Hassanizadeh, S.M. (eds.) Upscaling Multiphase Flow in Porous Media, pp. 43–62. Springer, Netherlands (2005)

Khan, F., Enzmann, F., Kersten, M., Wiegmann, A., Steiner, K.: 3d simulation of the permeability tensor in a soil aggregate on basis of nanotomographic imaging and lbe solver. J. Soils Sediments **12**(1), 86–96 (2011)

Knackstedt, M., Sheppard, A., Nguyen, V., Arns, C., Sok, R., et al.: 3d imaging and characterization of the pore space of carbonate core; implications to single and two phase flow properties. In: SPWLA 47th Annual logging symposium. Society of Petrophysicists and Well-Log Analysts (2006)

Krotkiewski, M., Ligaarden, I.S., Lie, K.-A., Schmid, D.W.: On the importance of the Stokes-Brinkman equations for computing effective permeability in karst reservoirs. Commun. Comput. Phys. **10**, 1315–1332 (2011)

Mehmani, A., Prodanović, M.: The effect of microporosity on transport properties in porous media. Adv. Water Resour. **63**, 104–119 (2014)

Mostaghimi, P., Blunt, M.J., Bijeljic, B.: Computations of absolute permeability on micro-CT images. Math. Geosci. **45**, 103–125 (2013)

Neale, G., Nader, W.: Practical significance of Brinkman's extension of Darcy's law: coupled parallel flows within a channel and a bounding porous medium. Can. J. Chem. Eng. **52**(4), 475–478 (1974)

Noiriel, C., Bernard, D., Gouze, P., Thibault, X.: Hydraulic properties and microgeometry evolution accompanying limestone dissolution by acidic water. Oil Gas Sci. Technol. **60**(1), 177–192 (2005)

Paganin, D., David, P., Mayo, S.C., Gureyev, T.E., Miller, P.R., Wilkins, S.W.: Simultaneous phase and amplitude extraction from a single defocused image of a homogeneous object. J. Microsc. **206**(1), 33–40 (2002)

Patankar S.V.: Numerical Heat Transfer and Fluid Flow. Taylor & Francis, Washington DC (1980)

Prodanović, M., Mehmani, A., Sheppard, A.P.: Imaged-based multiscale network modelling of microporosity in carbonates. Geol. Soc. Lond. Spec. Publ. **406**(1), 95–113 (2015)

Sanchez, S., Ahlberg, P.E., Trinajstic, K.M., Mirone, A., Tafforeau, P.: Three-dimensional synchrotron virtual paleohistology: a new insight into the world of fossil bone microstructures. Microsc. Microanal. **18**(05), 1095–1105 (2012)

Scheibe, T.D., Perkins, W.A., Richmond, M.C., McKinley, M.I., Romero-Gomez, P.D.J., Oostrom, M., Wietsma, T.W., Serkowski, J.A., Zachara, J.M.: Pore-scale and multiscale numerical simulation of flow and transport in a laboratory-scale column. Water Resour. Res. **51**(2), 1023–1035 (2015)

Shabro, V., Torres-Verdín, C., Javadpour, F.: Numerical simulation of shale-gas production: from pore-scale modeling of slip-flow, knudsen diffusion, and langmuir desorption to reservoir modeling of compressible fluid. In: North American Unconventional Gas Conference and Exhibition (2011)

Slattery, J.C.: Single-phase flow through porous media. AIChE J. **15**(6), 866–872 (1969)

Spanne, P., Thovert, J.F., Jacquin, C.J., Lindquist, W.B., Jones, K.W., Adler, P.M.: Synchrotron computed microtomography of porous media: topology and transports. Phys. Rev. Lett. **73**(14), 2001 (1994)

Tam, C.K.W.: The drag on a cloud of spherical particles in low reynolds number flow. J. Fluid Mech. **38**(03), 537–546 (1969)

Tanino, Y., Blunt, M.J.: Capillary trapping in sandstones and carbonates: dependence on pore structure. Water Resour. Res. **48**, 1–13 (2012)

Thovert, J.-F., Adler, P.M.: Grain reconstruction of porous media: application to a bentheim sandstone. Phys. Rev. E **83**(5), 056116 (2011)

Trebotich, D., Graves, D.T.: An adaptive finite volume method for the incompressible Navier-Stokes equations in complex geometries. Commun. Appl. Math. Comput. Sci. **10**, 43–82 (2015)

Whitaker, S.: Flow in porous media I: a theoretical derivation of Darcy's law. Transp. Porous Media **1**, 3–25 (1986). doi:10.1007/BF01036523

Wildenschild, D., Sheppard, A.P.: X-ray imaging and analysis techniques for quantifying pore-scale structure and processes in subsurface porous medium systems. Adv. Water Resour. **51**, 217–246 (2013). 35th Year Anniversary Issue

Youssef, S., Bauer, D., Han, M., Bekri, S., Rosenberg, E., Fleury, M., Vizika-kavvadias, O.: Pore-network models combined to high resolution micro-ct to assess petrophysical properties of homogenous and heterogenous rocks. In: International Petroleum Technology Conference. (2008)

Zhan, X., Schwartz, L., Smith, W., Toksäz, N., Morgan, D.: Pore scale modeling of rock properties and comparison to laboratory measurements. In: SEG Houston 2009 international exposition and annual meeting. Society of Exploration Geophysicists (2009)